Trailing edge actuation for a bluff body at moderate yaw optimized with a genetic algorithm

Physics of Fluids

RESEARCH ARTICLE | DECEMBER 05 2023

Trailing edge actuation for a bluff body at moderate yaw optimized with a genetic algorithm

Z. X. Qiao (乔增熙) ; G. Minelli ; B. R. Noack ; S. Krajnović ; V. Chernoray

Physics of Fluids 35, 125108 (2023)
https://doi.org/10.1063/5.0174822

Physics of Fluids ARTICLE pubs.aip.org/aip/pof

Trailing edge actuation for a bluff body at moderate yaw optimized with a genetic algorithm

Cite as: Phys. Fluids **35**, 125108 (2023); doi: 10.1063/5.0174822
Submitted: 3 September 2023 · Accepted: 13 November 2023 · Published Online: 5 December 2023

View Online Export Citation CrossMark

Z. X. Qiao (乔增熙),[1,2,a] G. Minelli,[2] B. R. Noack,[3,4] S. Krajnović,[2] and V. Chernoray[2]

AFFILIATIONS

[1]School of Naval Architecture and Ocean Engineering, Guangzhou Maritime University, Guangzhou Jiaotong University (preparation), 510725 Guangzhou, People's Republic of China
[2]Department of Mechanics and Maritime Sciences (M2), Chalmers University of Technology, SE-412 96 Gothenburg, Sweden
[3]School of Mechanical Engineering and Automation, Harbin Institute of Technology, 518058 Shenzhen, People's Republic of China
[4]Hermann-Föttinger-Institut, Technische Universität Berlin, Müller-Breslau-Straße 8, D-10623 Berlin, Germany

[a)]Author to whom correspondence should be addressed: qzx2009@126.com

ABSTRACT

This experimental work is conducted to manipulate the wake to reduce aerodynamic drag using the actuations on the trailing edges of a bluff body at a yaw angle of 10°. Two loudspeakers are separately installed into the vertical trailing edges of the vertical base, creating a zero-net mass-flux jet through vertical slots. A maximum drag reduction of 2% and 1.5% is produced by the single actuation on the windward and leeward side, respectively. When the genetic algorithm is introduced to optimize the actuations on both sides, a drag reduction of 7% is obtained. Thus, the energy efficiency of the entire control system is greatly improved by 80% compared to the best single actuation. The underlying flow mechanism behind the effective parameters is proposed according to the analyses of the drag spectra and the hot-wire data measured with and without control. The genetic algorithm provides a promising optimization strategy for the better control performance of trailing edge actuation on a yawed bluff body. Furthermore, this strategy may have the engineering potential to reduce the drag of ground transport vehicles for a large range of operating conditions. Therefore, this research is expected to save energy consumption and improve traveling safety for the aerodynamic control of vehicles.

I. INTRODUCTION

The aerodynamic control of bluff bodies raises a fascinating engineering challenge to improve ground vehicle aerodynamics, which is generally influenced by a strong flow separation and an unsteady wake. The latter is of particular interest for energy saving to increase mileages, which is vital for new electrical vehicles. Over the past decades, active flow control has been a fast-growing and multidisciplinary technology to modify turbulent flows to achieve a low-drag state with high traveling stability. Meanwhile, the actuators have gradually become smaller, lighter, more independent of a propulsion system, and more energy-efficient.[1] Several literature reviews on active flow control of bluff bodies are already available (e.g., Refs. 2–4).

The flow around a bluff body exhibits complex characteristics, such as a turbulent boundary layer, shear-layer evolution, massive separation at the blunt edge, and a large recirculation region in the wake. The active control of the flow around a bluff body has mainly focused on regulating the flow separation on either the leading or the trailing edges (e.g., Refs. 5–14). Seifert *et al.*[5] used suction and oscillatory blowing at the top and bottom trailing edges of a bluff body, and the maximum drag reduction of 20% was obtained. Zhang *et al.*[13] deployed steady blowing at the edges of the rear window and vertical base of an Ahmed body, resulting in a 29% drag reduction. Minelli *et al.*[9,10] employed loudspeakers to generate zero-net mass-flux jets through vertical or streamwise slots at the front A-pillar of the bluff body, and the side recirculation bubble was successfully suppressed using an optimized control signal. However, the drag reduction effect remains unclear. Based on the same model, Minelli *et al.*[11] numerically indicated that only an 8% drag reduction was achieved despite the total suppression of the side recirculation bubble. However, a drag reduction of up to 20% was achieved when the superharmonic frequencies of natural vortex shedding were introduced to reduce the shedding motion in the wake. Therefore, it is very interesting to investigate the effect of the control frequencies on drag reduction if the present work moves the position of the zero-net mass-flux jets from the leading to the trailing edges, i.e., the direct-wake control approach.

The yaw angle plays a crucial role in computing the cycle-averaged drag coefficient for a bluff body traveling in a natural environment.[15] Potentially, even for very streamlined objects, a flow separation would occur at a large yaw angle.[16–18] Once a yaw angle is introduced, the wake structures bend from one side to the other and the flow separation behaves very differently.[19,20] The drag coefficient increases with the yaw angle rising from zero to 30°.[20,21] However, less attention has been paid to controlling the bluff body flows at a yaw angle. Li *et al.*[22] used pulsed jets on either the windward or leeward trailing edge to reduce the drag of a simplified car model at a 5° yaw angle. They found that the optimal single frequency, applied to the windward trailing edge, resulted in a drag reduction of 6%, while the drag increased by 4% for the same frequency on the leeward trailing edge. Unlike their actuations, the zero-net mass-flux jets in this paper may have a great impact on the drag reduction of a yawed bluff body with a limited amount of energy for actuation.

Machine learning control (MLC) has been proposed recently to manipulate a bluff-body flow by optimizing the actuation parameters.[23–25] In this context, the genetic algorithm is a powerful technique for MLC that searches the effective parameters from a rich set of possible control laws.[26] Some works have been reported in the literature. Li *et al.*[12] used linear genetic programming to optimize the pulsed jets at all trailing edges of an Ahmed body and the optimal control parameters produced 33% of base pressure recovery and 22% of drag reduction. Inspired by their works, Minelli *et al.*[11] numerically implemented a generic algorithm to drive the blowing-suction actuation at the front edges of a bluff body model and obtained a maximum 20% drag reduction. Based on the same model at 10° yaw angle, Qiao *et al.*[27] experimentally employed a generic algorithm to optimize zero-net mass-flux jets at the front edges, and the optimal control parameters yielded a 20% drag reduction. These previous achievements show the high potential for improving control performance using a genetic algorithm. The primary topic of this paper is, therefore, to examine the capacity of a genetic algorithm when used for the actuations on the trailing edges of a yawed bluff body case.

In this study, the actuations on the trailing edges are optimized with a genetic algorithm to reduce the drag for a 10° yawed bluff body. The experimental setup, together with the wind tunnel facility, is shown in detail in Sec. II. The design of the genetic algorithm is described in Sec. III. The main results and the underlying flow physics are discussed in Secs. IV and V, respectively. The main conclusions are drawn in the final section.

II. EXPERIMENTAL DETAILS

A. The experimental setup

Experiments were conducted in a closed-circuit wind tunnel at Chalmers University of Technology, with a test section of 3.0 m in length, 1.8 m in width, and 1.25 m in height. The free-stream wind speed could be changed between 0 and 60 m/s. As shown in Fig. 1, a 0.36-m-long bluff body has a cross section area of 0.4 m wide and 0.4 m high, and has a radius of $R = 0.02$ m at the leading edges (A-pillars). The cross section area of the bluff body is 0.16 m^2 and its root mean square value is denoted as $W = 0.4$ m. The overall dimensions of the bluff body are the same as those used in Refs. 9, 10, and 27 except for the position of the actuators, which moves from the leading to the trailing edges. Cooper[28] proposed that the effect of front-edge roundness ($=R/W$) on aerodynamic drag is strongly influenced by both the yaw angle and the Reynolds number for bluff ground vehicles. In other words, at a fixed W, there is an optimal R to prevent local separation on the surface and to minimize aerodynamic drag at different yaw angles for every Reynolds number. However, it is unpractical to vary R for bluff vehicles while traveling at different yaw angles and Reynolds numbers. Moreover, the shape of bluff vehicles is often predefined based on legislative requirements, esthetics, and the ability to manufacture these vehicles, e.g., the outer dimensions of trucks.[7] Therefore, the present study is carried out to optimize aerodynamic drag using the active control at fixed R/W and yaw angles, which is useful for real applications. The yaw angle is set as 10° for the bluff body shown in Fig. 1, resulting in the blockage ratio of ~7%. A NACA airfoil is used to connect the bluff body to the force balance and remains at a zero angle of attack to minimize the aerodynamic drag [Figs. 1(a) and 1(c)]. The separation between the bluff body and the wind tunnel wall is 0.25 m. The coordinate system (x, y, z) is presented in Fig. 1, where x is the streamwise direction and its origin, o, is at the crossover point between the streamwise diameter of the force balance and the rear vertical base of the bluff body. The y is the lateral direction. The z is the vertical direction with the zero point at the midpoint of the rear vertical base.

Measurements were performed at a free-stream velocity of $U_\infty = 19$ m/s, with a turbulence intensity of 0.07%, corresponding to a Reynolds number of $Re = 4.7 \times 10^5$ based on W and U_∞. As presented in Fig. 1(c), two hot-wire probes were mounted on the computer-controlled traversing mechanism and traversed the wake to measure the flow behaviors with or without control. The sensing element of each hot-wire probe, made of tungsten, was 5 μm in diameter and 1.25 mm in length. These probes were operated on a constant temperature circuit (Dantec 56C01 CTA), with an over-heat ratio of 1.7. The measured signals from the hot-wire probes were filtered at a cutoff frequency of 3 kHz and sampled at a frequency of 10 kHz. These settings were high enough to capture the frequencies in the wake structures, e.g., the natural vortex shedding frequency of $f^* = 0.21$ or $f = 10$ Hz at the zero-yaw angle.[11] In this paper, f represents the frequency and the superscript "*" denotes the normalization by W and/or U_∞, e.g., $f^* = fW/U_\infty$ and $U^* = U/U_\infty$ (U is the streamwise velocity). A total of 432 points were collected to reproduce a 2 D map for the streamwise velocities in the wake, where the sampling duration was 15 s at each point.

B. Actuation

As shown in Fig. 1(c), two loudspeakers (Wavecor SW182BD02-01) are separately installed at the vertical trailing edges of the rear vertical base to produce the blowing and suction of air flow. A splitting plate is used to eliminate the possible interaction between the two vibrating loudspeakers. The loudspeaker is characterized by its maximum output power of 62 W and its impedance of 8 Ohm. Each speaker is connected to one channel of a power amplifier (ALTO MAC 2.4 stereo) and works independently. The amplification is set as $k_a = 53$ for the amplifier. The control signal in each channel comes from a LabVIEW platform via a 16-bit digital-to-analog (D/A) converter. There is a vertical slot of 1 mm wide and 330 mm long on each

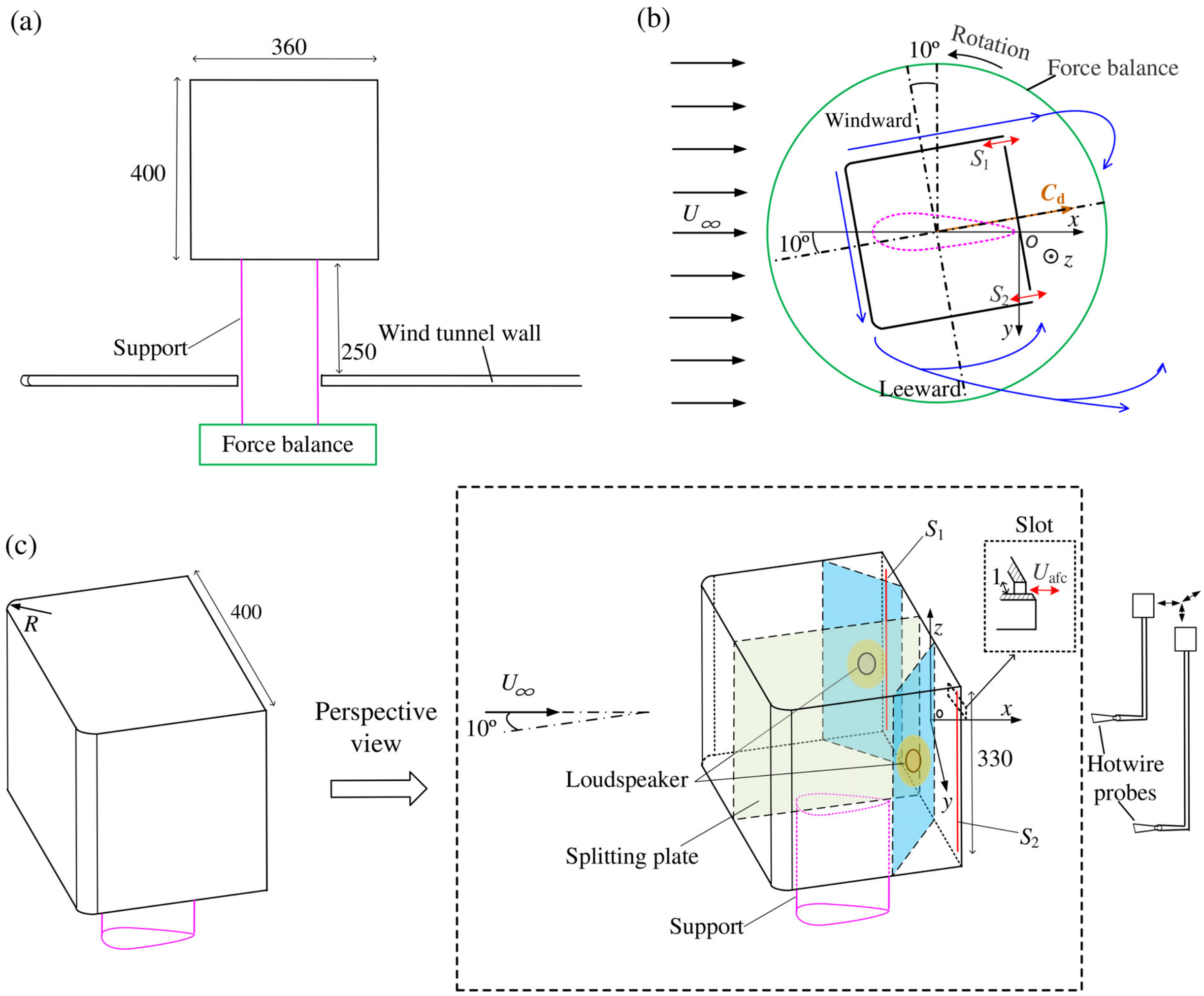

FIG. 1. (a) Wind tunnel and typical model geometries of the bluff body; (b) the top view of the bluff body at a 10° yaw angle; and (c) schematic of the experimental arrangement and a bluff body at a yaw angle of 10°, including two downstream actuators (S_1, S_2), a test section of wind tunnel, and two hot-wire probes. The dimensions of the bluff body are expressed in millimeters. The red arrows represent the actuated position, and the blue lines denote the flow separation around the bluff body. A splitting plate is used to eliminate the flow interaction between two actuators.

vertical trailing edge through which the actuation takes place [Fig. 1(c)]. The same actuated location resembles that used in Refs. 12 and 13, where the actuations have a substantial impact on wake dynamics and aerodynamic drag.

A calibrated hot-wire probe is placed 2 mm from the opening of the slot [Fig. 2(a)] to measure the strength of the actuation. The actuator is driven by a sinusoidal signal $S_o = k_a A_o \sin(2\pi f t)$, where A_o represents the amplitude and t denotes the time. To avoid possible damage to the actuators, the limitation is set to 0.4 V and 250 Hz ($f^* = 5.3$) for A_o and f, respectively. The real-time signal $U_{afc,t}$ exhibits a positively pronounced peak and a negative valley in every actuation cycle in Fig. 2(a), which corresponds to the blowing and suction phase, respectively.[9] Seifert *et al.*[1,5] suggested that the periodic excitation could accelerate and regulate the generation of large coherent structures and is vastly more effective than the steady blowing for separation control. As shown by the ensemble-averaged $\langle U_{afc,t}\rangle$ of $U_{afc,t}$ in Fig. 2(b), the resultant actuation is strongly dominated by a blowing flow, i.e., the synthetic or zero-net mass-flux jet.[29] The maximum value or the peak jet velocity of $\langle U_{afc,t}\rangle$ is denoted as U_{afc}, representing the strength of the actuation.[9] The iso-contour of U_{afc} is presented under different control parameters (f, A_o) in Fig. 2(c), where U_{afc} has different ranges with varying f. However, the control effect of f on drag reduction could be fully examined if U_{afc} has the same range at each f. Meanwhile, the range of U_{afc} is expected to be a large value to affect the incoming flow to a great extent. Therefore, the range has been arbitrary chosen as 0.63–2.63 and 0–1.1 for f^* and U^*_{afc}, respectively, as described in Fig. 2(c).

C. Aerodynamic force measurement

This experimental work aims to investigate the control effects on the drag F_d, which is against the vehicle's travel motion and to be

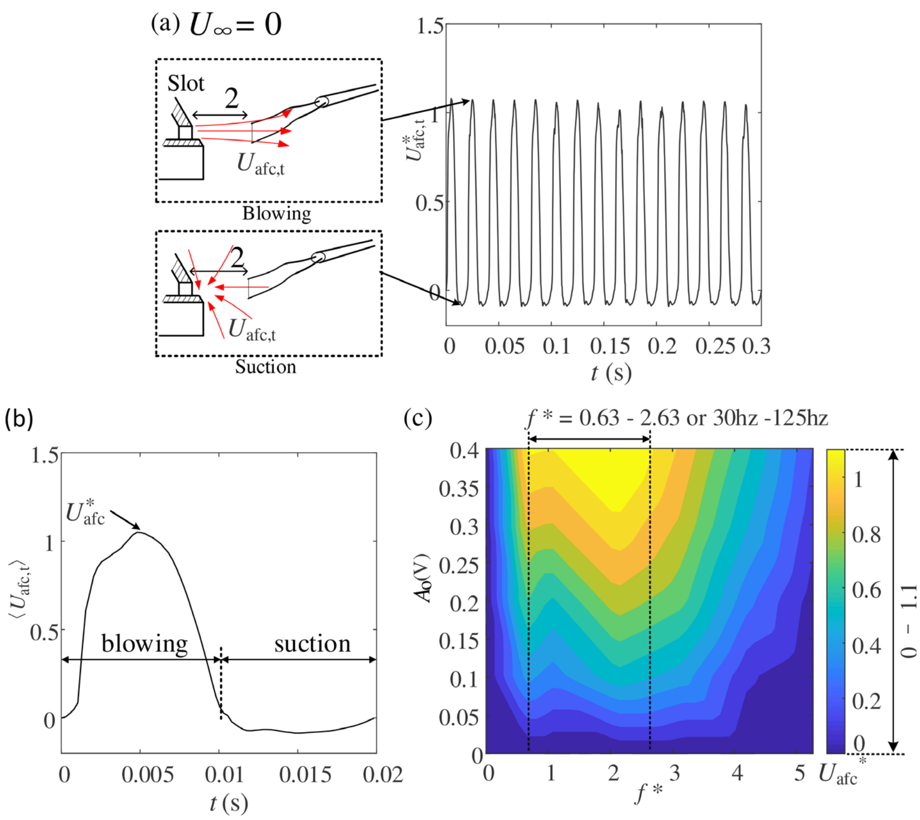

FIG. 2. (a) The real-time signal $U_{afc,t}$ including blowing and suction under the control parameters $(f^*, A_o) = (1.1, 0.4\,\text{V})$; (b) the ensemble-averaged $\langle U_{afc,t} \rangle$ of $U_{afc,t}$. U_{afc} is the peak jet velocity or maximum value of $\langle U_{afc,t} \rangle$; and (c) iso-contour of U_{afc} under different control parameters (f^*, A_o). The contour resolution is $\Delta = 0.1$. $U_\infty = 0$ m/s.

overcome by the propulsion system. The force balance is rotated counterclockwise to yield a yaw angle of 10° so that the F_d acting on the yawed bluff body can be directly measured [Fig. 1(b)]. The present measurement is confirmed by Refs. 22 and 30. The corresponding drag coefficient C_d is defined as follows:

$$C_d = \bar{F}_d / \left(W^2 \bar{P}_{dyn}\right). \tag{1}$$

Here, F_d is sampled with a frequency of 1000 Hz or $f^* = 21$. P_{dyn} represents the dynamic pressure and is measured using a Pitot-static tube placed in a free-stream wind. The overbar represents the time-averaged quantity in this paper. The C_d is 1.17 under the unactuated control, which is slightly higher than the value (=1.1) for the same model at a 10° yaw angle in Ref. 27. This difference is due to streamwise slots at the leading edges of the A-pillars in Ref. 27, which mitigate the A-pillar flow separation and reduce the drag coefficient.

III. GENETIC ALGORITHM OPTIMIZATION

As shown in Fig. 1(b), the flow separations are significantly different on the windward and leeward sides so that the actuations on two sides can play a very different role in improving the control performance of the bluff body. Therefore, Li *et al.*[22] separately performs the pulsed jets on the windward and leeward trailing edges on a simplified car model at a 5° yaw angle. They find that the actuations are much more effective on the windward trailing edge and that the optimal frequency results in a drag reduction of 6%. Based on this investigation, we are simultaneously using two different sinusoidal signals to separately control the actuations on the S_1 and S_2 sides to maximize the drag reduction. The control law b is defined as follows in Fig. 3:

$$\begin{cases} b_{S_1} = U_{afc1} \sin(2\pi f_1 t), \\ b_{S_2} = U_{afc2} \sin(2\pi f_2 t), \end{cases} \tag{2}$$

where b_{S_1} and b_{S_2} are the control laws for the S_1 and S_2 actuation, respectively. U_{afc1} and U_{afc2} are the peak jet velocities. f_1 and f_2 are the control frequencies. As depicted in Figs. 3 and 2(c), a matrix T uses a linear interpolation to transform U_{afc1} and U_{afc2} into the voltages of A_1 and A_2. Both A_1 and A_2 are further used to drive the actuations through the amplifier with the amplification of k_a (=53). The cost function J is defined by $[(C_d)_{on} - (C_d)_{off}]/(C_d)_{off}$, where the subscripts "*on*" and "*off*" denote the measurements with and without control, respectively. J is negative and its absolute value is the drag reduction. A decrease in J corresponds to an improvement on the drag reduction.

Following Ref. 26, the genetic algorithm is used to search the parameter space for the purpose of finding the optimal control law $b^\bigstar$, i.e., the parameters of f_1, f_2, U_{afc1}, and U_{afc2} to produce the global minimum J or the maximum drag reduction. As described in Fig. 3, the generation (nth) consists of N individuals or control laws and each individual accounts for generating r variables ($r = 4$), i.e., f_1, f_2, U_{afc1}, and U_{afc2}. Each variable is composed of the m binary genes (0 and 1) based on a binary encoding scheme.[31] In particular, the control individuals in the first generation ($n = 1$) are yielded using random initialization, where each parameter has an almost uniform probability in the given range.

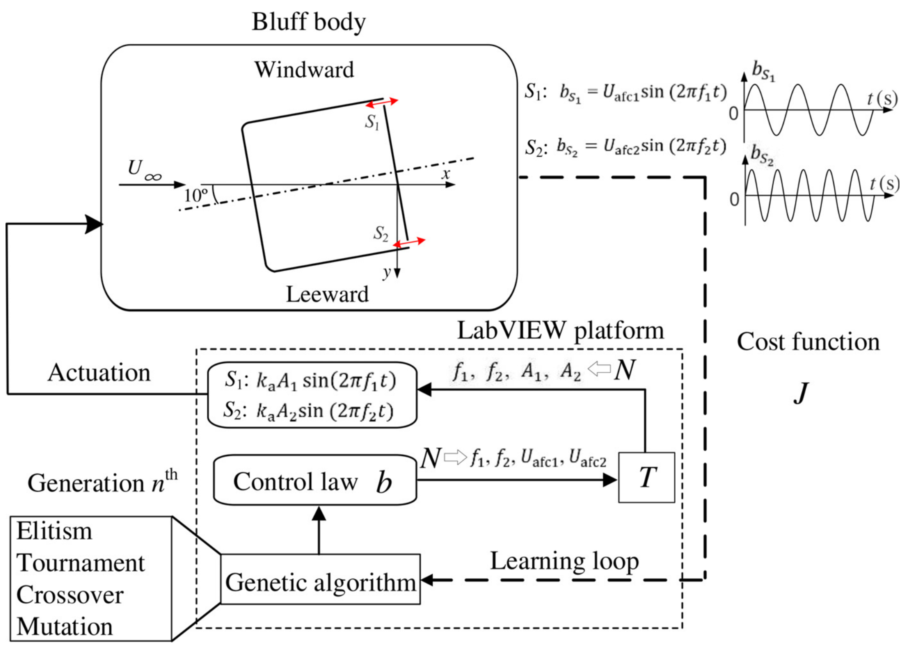

FIG. 3. Schematic diagram of a genetic algorithm system including the bluff body, two actuations (S_1, S_2), and the control laws of $b_{S_1} = U_{afc1}\sin(2\pi f_1 t)$ and $b_{S_2} = U_{afc2}\sin(2\pi f_2 t)$. The cost function J. T is a matrix, which transforms U_{afc1} and U_{afc2} into the voltages of A_1 and A_2, to further drive two actuations (S_1, S_2). k_a is the amplification of the amplifier. N is the number of individuals in each generation. $f_1^*,\ f_2^* \in [0.63,\ 2.63]$, $U_{afc1}^*,\ U_{afc2}^* \in [0, 1.1]$.

For the nth generation, every individual is experimentally evaluated to generate a J. Based on the N individuals and their corresponding J, the genetic algorithm performs the standard operations of elitism, tournament, crossover, and mutation to give rise to N individuals for the $(n+1)$th generation. Then, the genetic algorithm experimentally evaluates the new N individuals to obtain the same number of J. As such, the previous steps could be repeated for each generation unless the termination criterion has been reached, where the J converges to an uncertainty of less than 2% for the best individuals in the last five generations. The control parameters of the genetic algorithm are listed in Table I for simplicity. Readers may refer to the meaning and construction of the parameters in Sec. 3 of Ref. 26 for more details. N is set as 60 for each generation. As introduced in Sec. II B, the range was chosen as 0.63–2.63 for both f_1^* and f_2^*, and 0–1.1 for both U_{afc1}^* and U_{afc2}^*.

Control signals are generated on the LabVIEW platform and transferred to a National Instrument USB-9162 multifunction I/O Device to control the actuators. For every individual in each generation, the C_d is obtained at a sampling time of 8 s, with a rate of 1000 Hz, thereby calculating J. As the two actuations are controlled separately by two different control signals (b_{S_1} and b_{S_2}), the controller of the genetic algorithm is recognized as a multi-input-single-output system.

TABLE I. The control parameters used in the genetic algorithm.

Parameters	Value
Population size	$N = 60$
Variables per individual	$r = 4$
Binary size per variable	$m = 25$
Elitism	$i_e = 3$
Tournament size	$N_t = 5$
Tournament selection parameters	$P_{tour} = 0.75$
Crossover probability	$P_c = 0.8$
Mutation probability	$P_m = 1/m = 0.04$

IV. EXPERIMENTAL RESULTS AND DISCUSSION

A. Single actuation

The performance of the single actuation is examined to gain an understanding of the active control mechanism. The single actuation indicates that the actuation is controlled using a sinusoidal signal on only one side, while the other side is turned off. The single actuation on the windward and the leeward side is regarded as the S_1 and the S_2 control, respectively. As shown in Fig. 4(a), the minimum J is -2.0% in the neighborhood of $(f_1^*, U_{afc1}^*) = (1.05, 1.1)$ for the S_1 control. On the windward side, Li *et al.*[22] used pulsed jets for a simplified car model at a 5° yaw angle, and the optimal frequency resulted in a drag reduction of 6%. However, the same frequency, applied on their leeward trailing edge, contributed to a drag increase of 4%. In the current case, for the S_2 control on the leeward side [Fig. 4(b)], there are two minimum regions for $J = -1.5$% surrounding $(f_2^*, U_{afc2}^*) = (1.61, 1.1)$ and (2.63, 1.0). As a result, the present actuations could be beneficial for drag reduction on the windward and leeward sides while applying the appropriate control parameters. This kind of actuation is different from Ref. 22, where the actuation on the windward side is much more effective than on the leeward side and plays a dominant role in drag reduction. Furthermore, this observation implies that the genetic algorithm could optimize the control parameters to further improve the control performance while the actuations are combined on the two trailing edges.

B. Genetic algorithm control

The learning process has gradually improved the control performance for genetic algorithm control with increasing generation (n), as

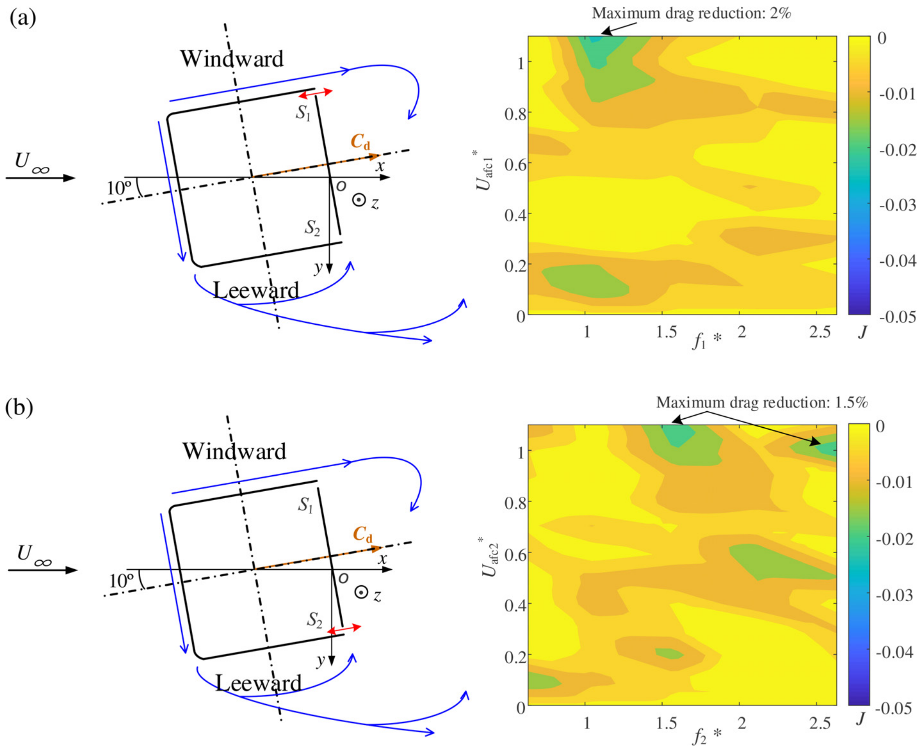

FIG. 4. (a) Iso-contours of J over U_{afc1} at different f_1 for the S_1 control. S_1: on, S_2: off; and (b) iso-contours of J over U_{afc2} at different f_2 for the S_2 control. S_1: off, S_2: on. The red arrows represent the actuated position, and the blue lines denote the flow separation around the bluff body. The contour resolution is $\Delta = 0.005$.

shown in Fig. 5. The individual index (i) is ranked from the lowest to the highest J value in each generation. The minimum J takes place at $i = 1$, which corresponds to the optimal or best control individual in every generation. As n increases, the minimum J gradually decreases to be close to -7% for $n \geq 10$, implying a good exploitation of the minimum drag value for genetic algorithm control.[11] Moreover, a wide range of J values is found in each generation, which indicates a good level of exploration from mutation probability (P_m). J gradually starts to overlap for the bar charts of all the individuals with increasing n, especially for $n \geq 10$.

The case yielding the minimum J for each generation is selected to examine the averaged J value and its standard deviation in Fig. 6. Each square on the line is tested at a sampling time of 16 s and 8 times over. The J values vary slightly for $n \geq 10$, and the lowest J is -7% at the generation $n = 24$, corresponding to the control parameters of $(f_1^*, U_{afc1}^*) = (0.96, 1.08)$ and $(f_2^*, U_{afc2}^*) = (1.38, 1.09)$. It is worthwhile pointing out that these control parameters produce a $J = -1.6\%$ and -1.1% for the S_1 [Fig. 4(a)] and the S_2 control [Fig. 4(b)], respectively. However, combined control on two sides produces a 7% drag reduction. This result also significantly outperforms the best single actuation of the S_1 and the S_2 control [2.0% of drag reduction in Fig. 4(a) and 1.5% in Fig. 4(b)]. These optimal control parameters slightly deviate from that of $(f_1^*, U_{afc1}^*) = (1.05, 1.1)$ in the S_1 control and $(f_2^*, U_{afc2}^*) = (1.61, 1.1)$ in the S_2 control, resulting from the balance control of the wake separations and vortex shedding on two sides, as explained later.

The learning process for control laws could be reflected in a proximity map following Refs. 11 and 32. Here, multi-dimensional scaling (MDS)[33] is used to optimally visualize high-dimensional data in a

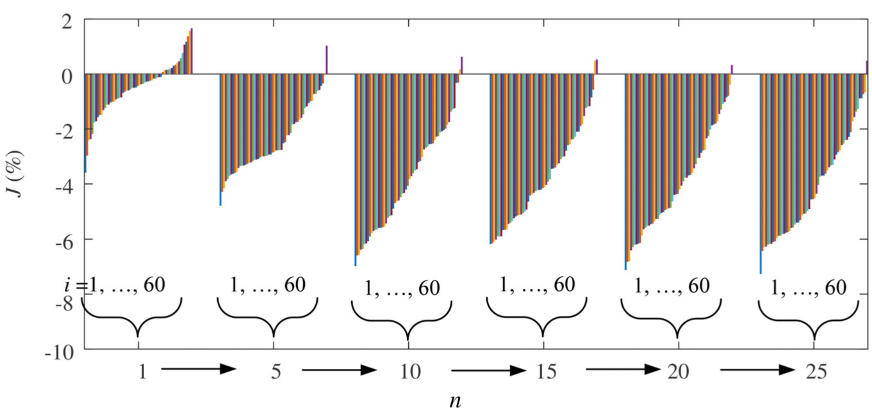

FIG. 5. Dependence of J on the individual index (i) for different generations (n). Each bar chart indicates that i is ranked from the lowest to the highest J value in each generation. Sixty individuals are tested for each of the 25 generations. For visual clarity, the symbols for every fifth generation are displayed between $n = 1$ and 25, i.e., $n = 1, 5, 10, \ldots, 25$.

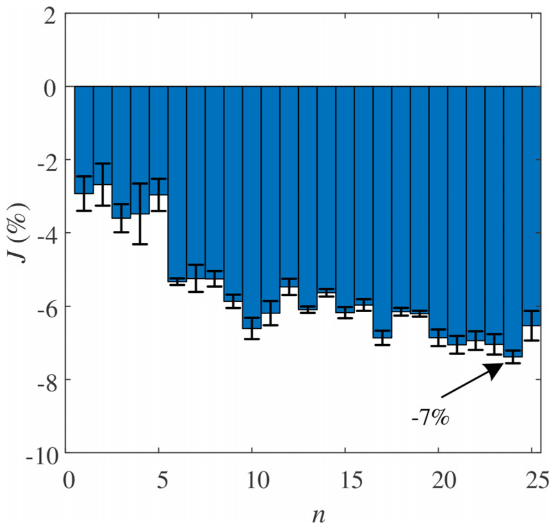

FIG. 6. J is for the best individual in each generation (n). The bar charts represent the average J values and the error bars denote the standard deviation.

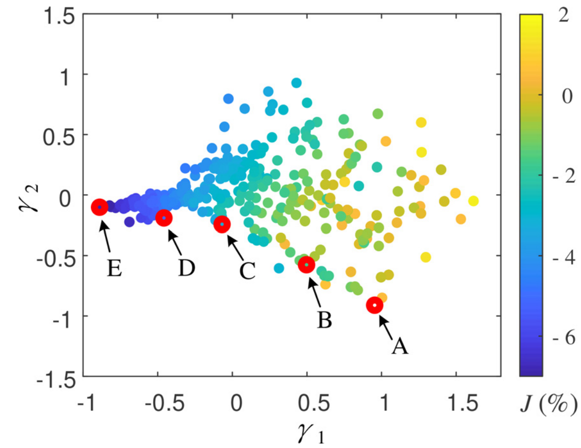

FIG. 7. Proximity map of the control individuals for generations ($n = 1$, 5, 10, 15, 20, and 24). Each dot represents a control individual and the distance between dots provides a measure for the dissimilarity between two control individuals. The black arrows and the red circles display five representative cases (A–E), and their details are listed in Table II.

low-dimensional feature space. The main idea is that every control individual is represented as a point in a two-dimensional feature plane (γ_1, γ_2), where the difference between the control individuals is indicated by the distance between feature vectors. For this purpose, the difference between two control laws b_l and b_q is given by a distance of $C_{l,q}$ with $1 \leq l,\ q \leq 25N$, where $25N$ is the total number of control individuals:

$$C_{l,q} = \sqrt{\sum_{j=1}^{2}\left|\frac{(f_j)_{b_l} - (f_j)_{b_q}}{f_{\max}}\right|^2 + \sum_{j=1}^{2}\left|\frac{(U_{afcj})_{b_l} - (U_{afcj})_{b_q}}{U_{afc,\max}}\right|^2} + \alpha\left|(J)_{b_l} - (J)_{b_q}\right|. \tag{3}$$

The first term is the averaged actuation difference between the lth and qth control individual, and the second represents a penalization based on the difference of their J. $f^*_{\max}$ and $U^*_{afc,\max}$ are the maximum values of 2.63 and 1.1 for the input frequencies (f_1^* and f_2^*) and amplitudes (U^*_{afc1} and U^*_{afc2}), respectively. The parameter α is chosen so that the maximum actuation difference in the first term is equal to the maximum difference of the second term for performance. See Ref. 32 for further details. Thus, the distance matrix is obtained by $C = (C_{l,q})_{1 \leq l,q \leq 25N}$. Figure 7 presents the proximity map of the control individuals in a two-dimensional plane of (γ_1, γ_2), where γ_1 and γ_2 are two eigenvectors corresponding to the two largest eigenvalues of C. Each dot represents a control individual colored with J and the distance between the dots provides a measure for the dissimilarity between two control individuals. For visual clarity, the data are displayed for generations $n = 1$, 5, 10, 15, 20, and 24. For $J \geq -4.5\%$, both γ_1 and γ_2 have a great impact upon improving control performance due to the scattered distribution correlating with J. Nevertheless, the dots tend to populate along a curve for $J < -4.5\%$, where the first feature coordinate γ_1 dominates the distribution of J values, while the second γ_2 plays a less important role in achieving the maximum drag reduction of $J = -7.0\%$ owing to its negligible variation correlating to the changing J. A similar learning process is commonly seen in MLC control, e.g., Refs. 11, 27, and 34. The black arrows and the red circles display five representative cases with letters between A and E, and their details are listed in Table II. Thus, the physical meaning of the feature coordinates γ_1 and γ_2 could be revealed by the following analysis. Cases B and D produce $J = -1.8\%$ and -5.1%, respectively, where f_1^*, f_2^*, and U^*_{afc1} have very similar values. The U^*_{afc2} increases from 0.28 to 0.93, which enhances the performance of f_2^* and is responsible for an increase of 3.3% (=5.1% − 1.8%) on drag reduction. Comparing the case E with D, one can also see the dominant effect of f_2^* on the drag reduction when the difference is negligible in f_1^*, f_2^* and U^*_{afc1}. The U^*_{afc2} varies from 0.93 (D case) to 1.09 (E case), which makes f_2^* more effective and contributes to an improvement of 1.9% (=7.0% − 5.1%) on drag reduction in the E case. These results suggest that the f_2^* and U^*_{afc2} are correlated with the coordinate γ_1. Thus, the S_2 control on the leeward side dominates the total control effect. The same observation was also made by Ref. 27, where the zero-net mass-flux jets, performed on the leeward side of the bluff body, led to a drag reduction of 17%, which was much higher than 2% on the windward side. On the other hand, the γ_2 is closely associated with the f_1^* and U^*_{afc1} for the S_1 control on the windward side, which facilitates the S_2 control to achieve the maximum drag reduction of 7.0% in the E case.

TABLE II. The control parameters and J values of five representative cases in Fig. 7.

Case	f_1^*	f_2^*	U^*_{afc1}	U^*_{afc2}	J (%)
A	0.74	1.46	1.04	0.01	−0.2
B	0.96	1.54	1.09	0.28	−1.8
C	0.93	1.49	1.07	0.76	−3.3
D	0.99	1.41	1.09	0.93	−5.1
E	0.96	1.38	1.08	1.09	−7.0

The evolution of the control individuals is illustrated with the probability density function (pdf) P of f_1, f_2, U_{afc1}, and U_{afc2} in Fig. 8. For clarity, control individuals are shown from generations of $n = 1$, 5, 15, and 24 and the optimal control parameters are marked using the vertical dash-and-dot lines. As introduced in Sec. III, the first generation randomly yields N individuals and each individual accounts for generating four parameters, i.e., f_1, f_2, U_{afc1}, and U_{afc2}. Therefore, each P exhibits an approximate flat shape in the first generation ($n = 1$). With increasing n, a significantly pronounced peak gradually occurs around the optimal control parameters of $U^*_{afc1} = 1.08$, $f^*_2 = 1.38$, and $U^*_{afc2} = 1.09$ on P for $n \geq 5$. Until $n \geq 15$, the peak emerges around the optimal $f^*_1 = 0.96$ on $P(f_1)$. This observation suggests that the genetic algorithm first finds the optimal parameters for (f_2, U_{afc2}) on the leeward side and then, tunes (f_1, U_{afc1}) on the windward side until the optimum control performance is obtained. This result provides an explanation for the better control performance at $n = 15$ than at $n = 5$, as shown in Fig. 5. Once the optimal parameters are found, increasing numbers of similar individuals can be generated from the former generation to keep the pronounced peak in a small range as depicted in Fig. 8. Again, the less pronounced peaks on $P(f_1)$, $P(U_{afc1})$, $P(f_2)$, and $P(U_{afc2})$ imply that the genetic algorithm continues to explore the search space using the mutation probability (P_m) but fails to find better minima of the J.

The optimal control individual has improved the energy efficiency (η) to a great extent compared to the single actuation. The η is defined as follows:

$$I_e = \frac{1}{2}\frac{B\rho}{T}\int_0^T \left[\left|U_{afc1}\sin(2\pi f_1 t)\right|^3 + \left|U_{afc2}\sin(2\pi f_2 t)\right|^3\right] dt, \tag{4}$$

$$I_0 = \frac{1}{2}\rho W^2 U_\infty^3 (C_d)_{off}|J|, \tag{5}$$

$$\eta = \frac{I_0}{I_e}, \tag{6}$$

where I_e is the power of the zero-net mass-flux jet consumed by the actuations and I_0 is the power saved by the drag reduction. B and ρ are the area of the slot and fluid density, respectively. T is the actuated duration of the S_1 and S_2 trailing edges. The η provides a measure for energy saved from the drag reduction as per unit energy consumed by the zero-net mass-flux jet. For the optimal control, I_e is 5.0 W and I_0 is 57.7 W, respectively, given $J = -7.0\%$ under (f^*_1, U^*_{afc1}) = (0.96, 1.08) and (f^*_2, U^*_{afc2}) = (1.38, 1.09). Apparently, this is a highly efficient control system with a η equal to 11.5. For the S_1 control, I_e and I_0 can be estimated as 2.6 and 16.6 W, respectively, given the best control performance $J = -2.0\%$ under (f^*_1, U^*_{afc1}) = (1.05, 1.1) presented in Fig. 4(a). Thus, η is 6.4. For the S_2 control, η is estimated as 4.8 using the same calculation for the best control performance in Fig. 4(b). As a result, η for the optimal control has been improved by 80% and 140% compared to the S_1 and the S_2 control, respectively. This observation further reveals that the genetic algorithm optimizes downstream actuations to greatly improve the drag reduction, thus outperforming the single actuation in terms of energy efficiency.

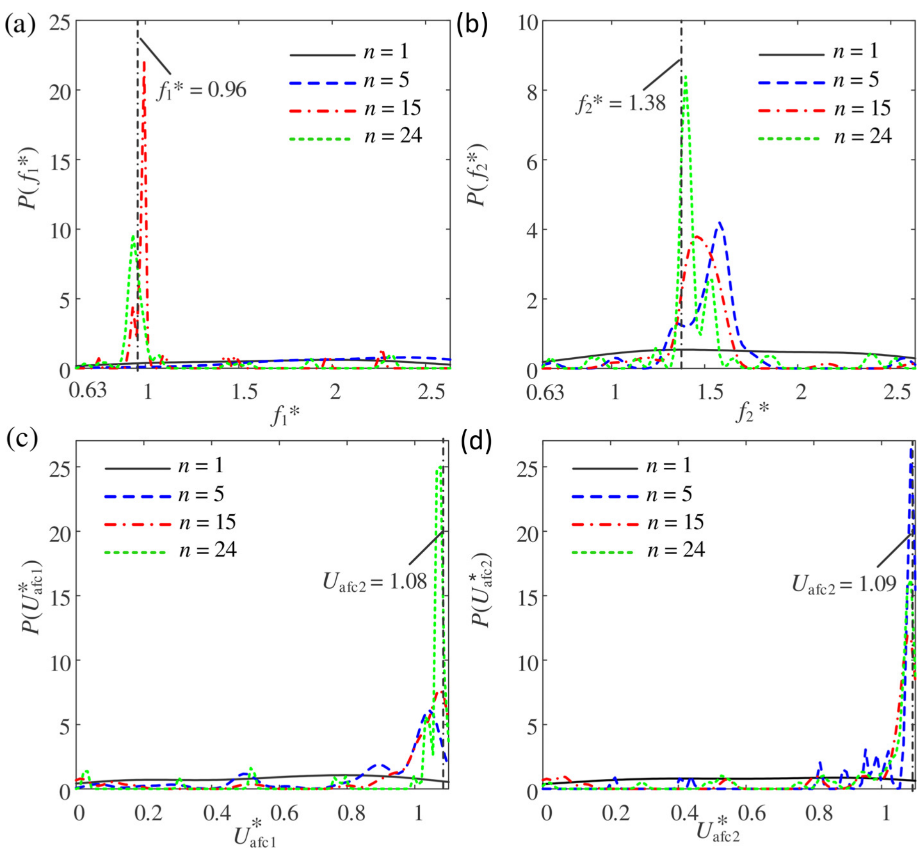

FIG. 8. The probability density function P of (a) f_1, (b) f_2, (c) U_{afc1}, and (d) U_{afc2} for the control individuals in the generations ($n = 1$, 5, 15, and 24). f^*_1, $f^*_2 \in [0.63, 2.63]$, U^*_{afc1}, $U^*_{afc2} \in [0, 1.1]$.

V. FLOW PHYSICS

The power spectra E of the drag coefficient (C_d) are well reflected in the frequency domain for cases under different observations as in Fig. 9(a). The natural frequencies are found in $f^* = 0.13$–0.14, with the pronounced peak for the bluff body mechanic system while it is activated with a collision at $U_\infty = 0$ m/s. For the collision case, the power spectra of F_d are displayed owing to $\bar{P}_{dyn} = 0$ in Eq. (1). It is interesting to note that the frequencies with the pronounced peak remain unchanged at $f^* = 0.13$–0.14 under no control case at $U_\infty = 19$ m/s. This coincidence further provides a strong validation for the correct measurement on the natural frequencies of the mechanical system. The peak values of the natural frequencies could be used to measure the stability of the mechanical system under the actuated case. Compared to the no control case, the peak at $f^* = 0.13$–0.14 has been reduced for the optimal control. This reduction implies that the actuations have stabilized the flow around the bluff body to weaken the vibration, as described in Fig. 9(b). As a result, the averaged C_d drops from 1.17 to 1.09 for the optimal control, thus achieving a drag reduction of 7%. Additionally, one can clearly see the second superharmonics $f^* = 1.92$ and 2.76 of the optimal control in Fig. 9(a), which are associated with the input control frequencies $f_1^* = 0.96$ and $f_2^* = 1.38$, respectively.

The distributions of the streamwise velocity U and its rms (root mean square) value $u_{\rm rms}$ provide crucial information for the flow behaviors in the wake of a bluff body. u represents the streamwise fluctuation velocity of U. Two calibrated hot-wire probes are used to measure U and $u_{\rm rms}$ at $(x/W, y/W) = (0$–$1.39, -0.80$ to $-0.20)$ on the windward side and $(x/W, y/W) = (0.11$–$1.50, 0.20$ to $0.80)$ on the leeward side at the plane of $z = 0$. The iso-contours of the velocity field are, therefore, made for the unactuated and three controlled cases, as illustrated in Figs. 10–12. For the S_1 or S_2 control, the actuations simply make use of the corresponding control parameters from the optimal control. With the present hot-wire measurement, we can explain why each side separately produces 1%–2% and together 7% of drag reduction.

Comparing the S_1 control to the no control case, the flow has been stabilized along the streamwise direction on the windward side, while the flow separation is suppressed on the leeward side as described in Figs. 10(a), 10(b), 11(a), and 11(b). This observation is responsible for 1.6% drag reduction under the S_1 control. For the windward side, the core area of the flow separation is between $y/W = -0.70$ and -0.50, where the maximum u^*_{rms} occurs [Figs. 11(a) and 11(b)]. A representative line is chosen as $y/W = -0.68$ throughout the core area of the flow separation. As shown in Figs. 10(a), 10(b), and 12(a), the $\bar{U}^*$ varies in the range of [0.86, 1.0] along $y/W = -0.68$ for the no control case while the range has been shrunk in $\bar{U}^* = 0.86$–0.95 for the S_1 control. The rms value of $\bar{U}^*$ along $y/W = -0.68$ has been reduced from 0.048 to 0.030 with a drop by 38% for the S_1 control. As x/W increases from 0 to 1.39 along $y/W = -0.68$, the u^*_{rms} gradually decreases from 0.25 to 0.18 for the no control case, while to 0.19 for the S_1 control in Figs. 11(a), 11(b), and 12(d). This result indicates that the S_1 control stabilizes the flow along the streamwise direction and improves the lateral stability on the windward side. This analysis agrees with Ref. 11, who performed upstream actuations at the leading edges of a bluff body to manipulate the wake dynamics and further suggested that the actuations significantly mitigated the shedding motion in the wake, therefore reducing the lateral vibration and contributing to a drag reduction. For the leeward side, the blue lines denote the core area of flow separation and the measured area locates in the inner flank of flow separation in Figs. 10(a), 10(b), 11(a), and 11(b). There is an increase on both $\bar{U}^*$ [Fig. 12(b)] and u^*_{rms} [Fig. 12(e)] over the range of $y/W = 0.60$–0.80 at $x/W = 0.11$ for the S_1 control. Moreover, both $\bar{U}^*$ [Fig. 12(c)] and u^*_{rms} [Fig. 12(f)] slightly go up over the range of $x/W = 0.82$–1.50 at $y/W = 0.2$. These results indicate that the core area of flow separation moves closer to the bluff body and the wake is suppressed on the leeward side for the S_1 control. For the flow over a square-back vehicle, the substantial wake diminution has been also observed by Refs. 35 and 36 to lead to the base pressure recovery and drag reduction. It is further inferred that the actuation, produced on the windward side for the S_1 control, stabilizes the flow along the streamwise direction, thus resulting in a deflection of the shear layer to reduce the separation region on the leeward side.

The drag reduction is 1.1% and 7.0% for the S_2 control and the optimal control, respectively, which also results from the stabilized

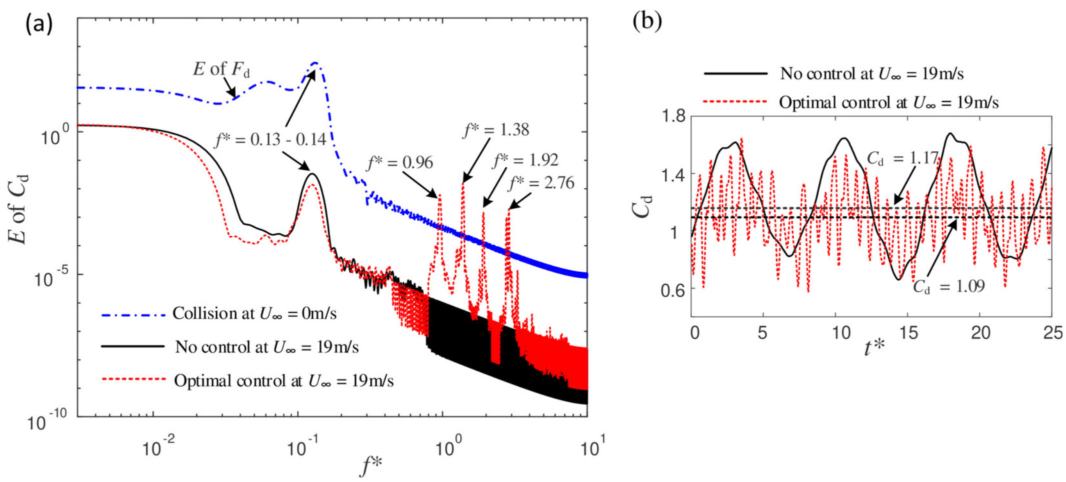

FIG. 9. (a) Power spectra of C_d under different control parameters (refer to the key) and (b) Time histories of drag coefficient C_d. Optimal control: $(f_1^*, U^*_{afc1}) = (0.96, 1.08)$ and $(f_2^*, U^*_{afc2}) = (1.38, 1.09)$.

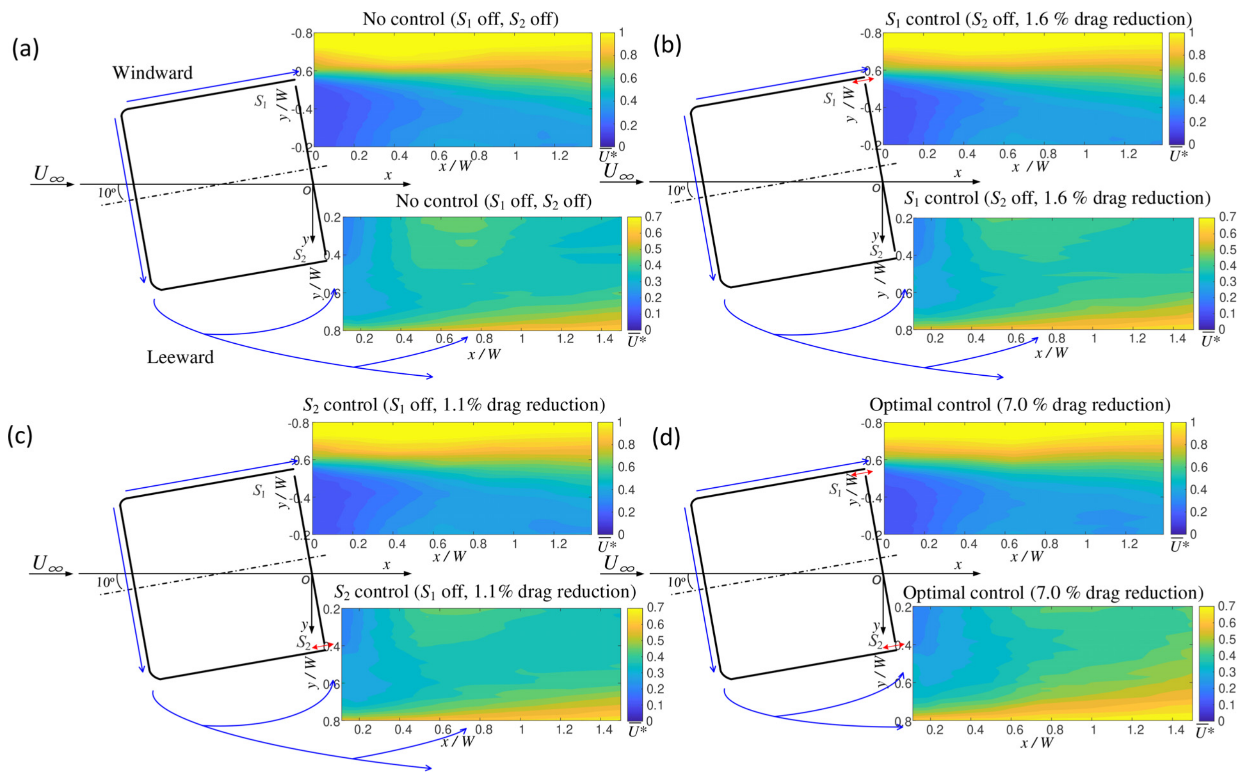

FIG. 10. Iso-contours of $\bar{U}$ in the wake of a bluff body: (a) No control: the actuators are unactuated (S_1: off, S_2: off); (b) S_1 control. S_1: (f_1^*, U_{afc1}^*) = (0.96, 1.08), S_2: off; (c) S_2 control. S_1: off, S_2: (f_2^*, U_{afc2}^*) = (1.38, 1.09); and (d) optimal control. S_1: (f_1^*, U_{afc1}^*) = (0.96, 1.08), S_2: (f_2^*, U_{afc2}^*) = (1.38, 1.09). The red arrows represent the actuated position, and the blue lines denote the flow separation around the bluff body. The contour resolution is $\triangle = 0.04$. $U_\infty = 19$ m/s.

flow along the streamwise direction on the windward side and the suppressed flow separation on the leeward side, as shown in Figs. 10(c), 10(d), 11(c), 11(d), and 12. For the windward side, both $\bar{U}^*$ and u_{rms}^* are nearly same for the S_1 and the S_2 control along the representative line of $y/W = -0.68$ in Figs. 10(b), 10(c), 11(b), 11(c), 12(a), and 12(d). For the leeward side, the S_1 control is in good agreement with the S_2 control on both the $\bar{U}^*$ and u_{rms}^* in Figs. 12(b), 12(e), 12(c), and 12(f). Thus, the drag reduction of the former control (1.6%) is very similar with the latter control (1.1%). Note that the actuation is produced on the leeward side for the S_2 control and the windward side the S_1 control. Therefore, these results mean that, in contrast to the S_1 control, the S_2 control results in a suppression of the separation region on the leeward side, making the flow more stable along the streamwise direction than the no control case on the windward side. It is worthwhile pointing out that the position of upstream separation points slightly varies for the S_1 and S_2 control on both windward and leeward sides. This observation is ascribed to the same distributions of $\bar{U} - x$ ($y/W = -0.68$ and 0.2) and $\bar{U} - y$ ($x/W = 0.11$) between the two controls in the wake [Figs. 12(a)–12(c)]. Furthermore, the drag reductions are small and approximately equal for the S_1 and S_2 control, implying that the present direct-wake control approach brings a negligible effect on the position of upstream separation points for the bluff body. When the S_2 control is combined with the S_1 control, the optimal control makes full use of the actuations on both the windward and leeward sides and, thus, greatly enhances the control performance. The optimal control is in good agreement with the S_1 or S_2 control on the distribution of $\bar{U}^*$ [Figs. 10(b)–10(d) and 12(a)] and u_{rms}^* [Figs. 11(b)–11(d) and 12(d)] on the windward side where the flow is stabilized along the streamwise direction. For the leeward side, the optimal control brings an increase on both $\bar{U}^*$ [Fig. 12(b)] and u_{rms}^* [Fig. 12(e)] over the range of $y/W = 0.50$–0.80 at $x/W = 0.11$ compared to the S_1 or S_2 control. At $y/W = 0.2$, both $\bar{U}^*$ [Fig. 12(c)] and u_{rms}^* [Fig. 12(f)] exhibit a higher value over $x/W = 0.85$–1.50 for the optimal control than the S_1 or S_2 control. This measurement indicates that the most significant reduction in flow separation takes place on the leeward side for the optimal control [Figs. 10(d) and 11(d)], contributing to the drag reduction.[12] However, there is a decrease on $\bar{U}^*$ over $x/W = 0.11$–0.85, revealing that a slight enlargement of flow separation occurs on the vertical trailing edge of the rear vertical base due to the actuation. This observation has a negative impact on drag reduction. Nevertheless, the compromise leads to the highest drag reduction of 7% for the optimal control, which is 4.4–6.4 times that for the S_1 and S_2 control. This result further suggests that the stabilization of the flow on the windward side plays almost the same role as the suppression of the separation region on the leeward side in the drag reduction. For the optimal control, the combination of the S_1 and S_2 control stabilizes the flow on the windward side and reduces the separation region on the leeward side at the same time, thus significantly improving the control performance.

Insight may be gained into the control mechanism by examining the vortex shedding in the wake of the bluff body. The fluctuating

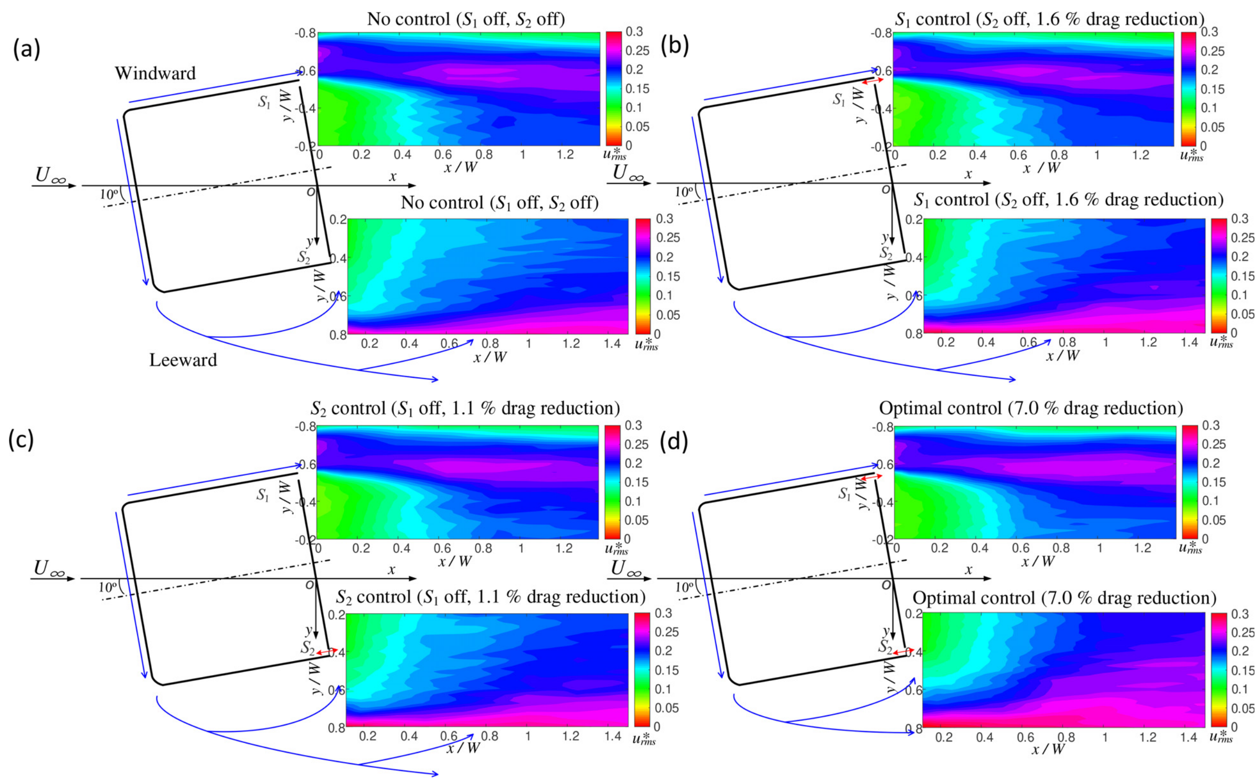

FIG. 11. Iso-contours of u_{rms} in the wake of a bluff body. Refer to Fig. 10 for the control parameters in (a), (b), (c), and (d). The contour resolution is $\triangle = 0.01$. $U_\infty = 19$ m/s.

velocities u_H and u_K are measured simultaneously from the two calibrated hot-wire probes, which are located at the H point of $(x/W, y/W) = (1.39, -0.5)$ on the windward side and the K point of $(x/W, y/W) = (1.50, 0.5)$ on the leeward side (Fig. 13). The separation between the H and K point is W in the y direction. There is a pronounced peak at $f^* = 0.15$ on the power spectra E for both u_H and u_K under the no control case [Figs. 13(a) and 13(b)]. The same observation is further clarified for the co-spectra $Co_{u_H u_K}$ between u_H and u_K in Fig. 13(c). The $f^* = 0.15$ is identified as the nature vortex shedding frequency, which is very close to the Strouhal number $f^* \approx 0.13$ for the square cylinder at $\mathrm{Re} > 2 \times 10^4$ in Refs. 37 and 38. The small discrepancy may be ascribed to the length-to-width ratio of 0.9 for the present bluff body, which is slightly less than 1. Compared to the no control case, the peak completely disappears at $f^* = 0.15$ on both E and $Co_{u_H u_K}$ for the optimal control and the vortex shedding motion has been significantly suppressed in the wake. This is consistent with the observation on a drag reduction for the bluff body.[11,39] In other words, the trailing edge actuations stabilize the flow on the windward side and reduce the separation region on the leeward side, resulting in drag reduction and the suppression of the vortex shedding motion in the wake.

VI. CONCLUSION

This work experimentally aims to perform the actuations on the trailing edges to reduce the drag for a bluff body at a yaw angle of 10°. Two loudspeakers are separately installed into the vertical trailing edges of the vertical base, creating a zero-net mass-flux jet through vertical slots. The maximum drag reduction is 2% and 1.5% for the single actuation on the windward and leeward side, respectively. Furthermore, the single actuation produces an energy efficiency of 6.4 and 4.8 on the windward and leeward side, respectively, implying the high efficiency of this control strategy.

A genetic algorithm is introduced to optimize the actuations on the trailing edges. Two sinusoidal signals are used to separately control the actuators on the windward and leeward side. Therefore, four parameters have been investigated, i.e., two frequencies (f_1, f_2) and two peak jet velocities (U_{afc1}, U_{afc2}). The maximum reduction in C_d is 7% for the optimal control, 5% higher than 2% for the best single actuation. Thus, the optimal control obtains an energy efficiency value of 11.5, an 80% improvement compared to the best single actuation. The result outperforms the actuations on the front edges of a yawed bluff body, where only 3% drag reduction of increase (from 17% to 20%) is achieved in our previous work.[27] This is ascribed to the different locations of the upstream and downstream actuations. The upstream actuations could interact with an easy-to-manipulate boundary layer and further influence the wake behaviors, while the downstream actuations have a direct impact on the flow characteristics in the wake.[9,11] This observation poses a great challenge to control strategies for improving the performance of the downstream actuations. As a result, the genetic algorithm tunes the control parameters based on a trial-and-error method and provides a useful tool for substantially enhancing the control performance of the downstream actuations.

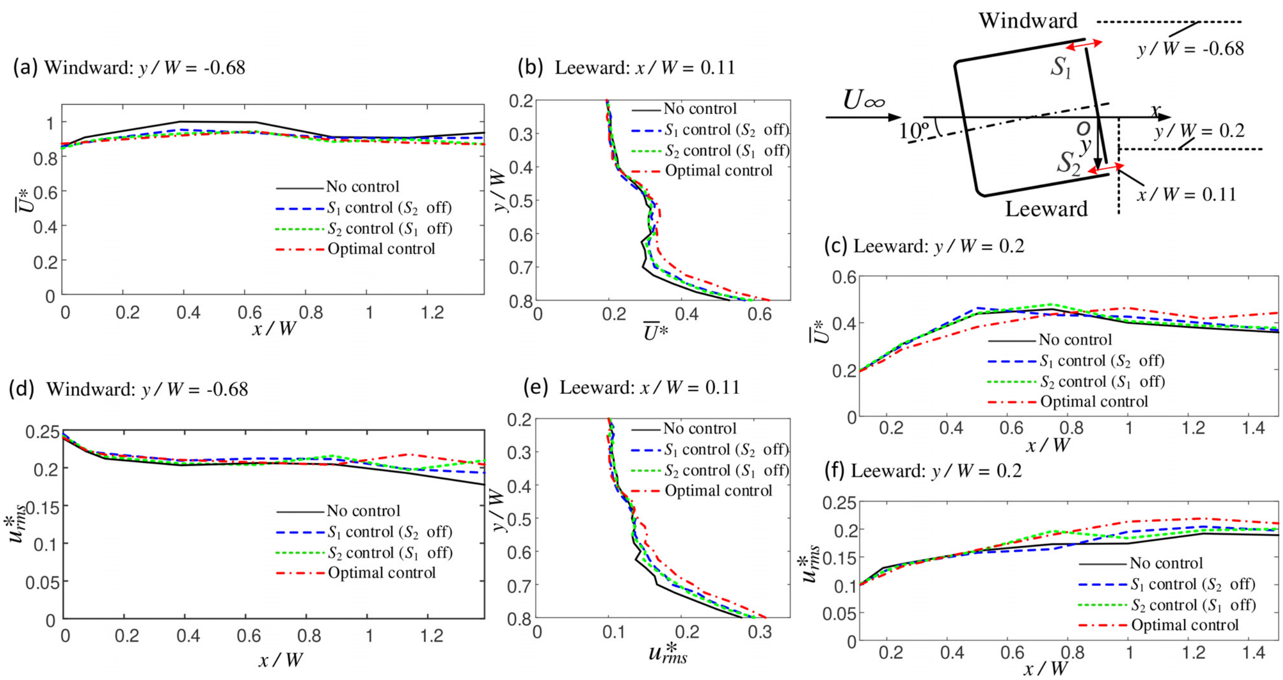

FIG. 12. Distributions of (a) $\bar{U} - x$ at $y/W = -0.68$, (b) $\bar{U} - y$ at $x/W = 0.11$, (c) $\bar{U} - x$ at $y/W = 0.2$, (d)$u_{rms} - x$ at $y/W = -0.68$, (e)$u_{rms} - y$ at $x/W = 0.11$, and (f)$u_{rms} - x$ at $y/W = 0.2$. The control parameters are as in Fig. 10. $U_\infty = 19$ m/s.

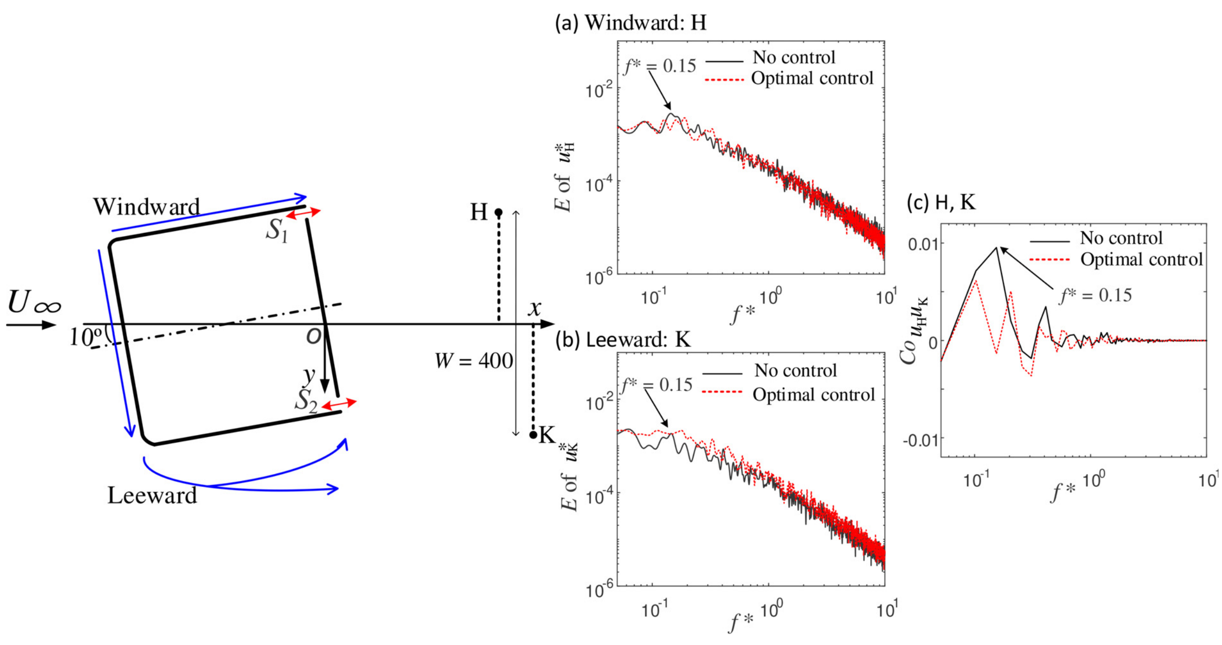

FIG. 13. (a) Power spectra E of u_H at the H point of $(x/W, y/W) = (1.39, -0.5)$ on the windward side; (b) power spectra E of u_K at the K point of $(x/W, y/W) = (1.50, 0.5)$ on the leeward side; and (c) co-spectra $Co_{u_H u_K}$ between u_H and u_K, measured simultaneously from the two calibrated hot-wire probes. The control parameters are as in Fig. 10. $U_\infty = 19$ m/s.

The measured data from the force balance and hot wires are analyzed. A number of observations are made. First, the power spectra of the drag suggest that the optimal control has substantially minimized the energy on the natural frequencies $f^* = 0.13$–0.14 of the bluff body mechanical system, further suppressing the vibration of the bluff body and stabilizing the flow in the wake. Second, the S_1 control stabilizes the flow along the streamwise direction on the windward side, and further results in a reduction of flow separation on the leeward side. Thus, the drag has been reduced for the bluff body. For the S_2 control, the actuation, produced on the leeward side, is used to reduce the separation region in the wake and obtains a drag reduction. Finally, the optimal control takes full advantage of actuations on both the windward and leeward sides to lead to the maximum suppression on the separation region and vortex shedding motion, thus obtaining the highest drag reduction.

For future work, we aim to develop a genetic algorithm strategy to combine the leading with trailing actuations, thus making a complete flow optimization for the bluff body.

ACKNOWLEDGMENTS

The current work was funded and supported by Chalmers University of Technology on experimental facilities provided by Chalmers Laboratory of Fluids and Thermal Sciences. This work was also supported by the National Science Foundation of China (NSFC) through Grant Nos. 12002098, 12172109, and 12172111, by the Guangdong Basic and Applied Basic Research Foundation under Grant No. 2022A1515011492, and by the Shenzhen Science and Technology Program under Grant No. JCYJ20220531095605012.

AUTHOR DECLARATIONS

Conflict of Interest

The authors have no conflicts to disclose.

Author Contributions

Zengxi Qiao: Data curation (equal); Formal analysis (equal); Investigation (equal); Methodology (equal); Writing – original draft (equal). **Guglielmo Minelli:** Conceptualization (equal); Formal analysis (equal); Writing – review & editing (equal). **Bernd R. Noack:** Conceptualization (equal); Writing – review & editing (equal). **Sinisa Krajnović:** Conceptualization (equal); Supervision (equal); Writing – review & editing (equal). **Valery G. Chernoray:** Conceptualization (equal); Supervision (equal); Writing – review & editing (equal).

DATA AVAILABILITY

The data that support the findings of this study are available from the corresponding author upon reasonable request.

REFERENCES

[1] A. Seifert, D. Greenblatt, and I. J. Wygnanski, "Active separation control: An overview of Reynolds and Mach numbers effects," Aerosp. Sci. Technol. **8**(7), 569 (2004).
[2] H. Choi, W. P. Jeon, and J. Kim, "Control of flow over a bluff body," Annu. Rev. Fluid Mech. **40**, 113 (2008).
[3] H. Choi, J. Lee, and H. Park, "Aerodynamics of heavy vehicles," Annu. Rev. Fluid Mech. **46**, 441 (2014).
[4] V. Oruc, "Strategies for the applications of flow control downstream of a bluff body," Flow Meas. Instrum. **53**, 204 (2017).
[5] A. Seifert, O. Stalnov, D. Sperber, G. Arwatz, V. Palei, S. David, I. Dayan, and I. Fono, "Large trucks drag reduction using active flow control," in *Aerodynamics of Heavy Vehicles II: Trucks, Buses, and Trains* (Springer, Berlin, Heidelberg, 2009), pp. 115–133.
[6] S. Aubrun, J. McNally, F. Alvi, and A. Kourta, "Separation flow control on a generic ground vehicle using steady microjet arrays," Exp. Fluids **51**(5), 1177 (2011).
[7] H. J. Schmidt, R. Woszidlo, C. N. Nayeri, and C. O. Paschereit, "Drag reduction on a rectangular bluff body with base flaps and fluidic oscillators," Exp. Fluids **56**(7), 151 (2015).
[8] G. Minelli, S. Krajnović, B. Basara, and B. R. Noack, "Numerical investigation of active flow control around a generic truck A-pillar," Flow. Turbul. Combust. **97**(4), 1235 (2016).
[9] G. Minelli, E. A. Hartono, V. Chernoray, L. Hjelm, and S. Krajnović, "Aerodynamic flow control for a generic truck cabin using synthetic jets," J. Wind Eng. Ind. Aerodyn. **168**, 81 (2017).
[10] G. Minelli, M. Tokarev, J. Zhang, T. Liu, V. Chernoray, B. Basara, and S. Krajnović, "Active aerodynamic control of a separated flow using streamwise synthetic jets," Flow. Turbul. Combust. **103**(4), 1039 (2019).
[11] G. Minelli, T. Dong, B. R. Noack, and S. Krajnović, "Upstream actuation for bluff-body wake control driven by a genetically inspired optimization," J. Fluid Mech. **893**, A1 (2020).
[12] R. Li, B. R. Noack, L. Cordier, J. Borée, and F. Harambat, "Drag reduction of a car model by linear genetic programming control," Exp. Fluids **58**(8), 103 (2017).
[13] B. F. Zhang, K. Liu, Y. Zhou, S. To, and J. Y. Tu, "Active drag reduction of a high-drag Ahmed body based on steady blowing," J. Fluid Mech. **856**, 351 (2018).
[14] M. Tokarev, G. Minelli, J. Zhang, B. R. Noack, V. Chernoray, and S. Krajnović, "PIV measurements around a generic truck model in active flow control experiments," in 13th International Symposium on Particle Image Velocimetry (ISPIV), Munich, Germany, 2019.
[15] J. Howell, M. Passmore, and S. Windsor, "A drag coefficient for test cycle application," SAE Int. J. Passeng. Cars - Mech. Syst. **11**, 447 (2018).
[16] Y. Fan, V. Parezanović, and O. Cadot, "Wake transitions and steady-instability of an Ahmed body in varying flow conditions," J. Fluid Mech. **942**, A22 (2022).
[17] R. D. Xue, X. H. Xiong, X. B. Li, and G. Chen, "Influence of turbulent incoming flow on aerodynamic behaviors of train at 90° yaw angle," Phys. Fluids **35**, 015121 (2023).
[18] H. Viswanathan, "Aerodynamic performance of several passive vortex generator configurations on an Ahmed body subjected to yaw angles," J. Braz. Soc. Mech. Sci. Eng. **43**, 131 (2021).
[19] M. Grandemange, O. Cadot, A. Courbois, V. Herbert, D. Ricot, T. Ruiz, and R. Vigneron, "A study of wake effects on the drag of Ahmed's squareback model at the industrial scale," J. Wind Eng. Ind. Aerodyn. **145**, 282 (2015).
[20] F. J. Bello-Millan, T. Mäkelä, L. Parras, C. Del Pino, and C. Ferrera, "Experimental study on Ahmed's body drag coefficient for different yaw angles," J. Wind Eng. Ind. Aerodyn. **157**, 140 (2016).
[21] E. Guilmineau, O. Chikhaoui, G. Deng, and M. Visonneau, "Cross wind effects on a simplified car model by a DES approach," Comput. Fluids **78**, 29 (2013).
[22] R. Li, J. Borée, B. R. Noack, L. Cordier, and F. Harambat, "Drag reduction mechanisms of a car model at moderate yaw by bi-frequency forcing," Phys. Rev. Fluids **4**(3), 034604 (2019).
[23] S. L. Brunton, B. R. Noack, and P. Koumoutsakos, "Machine learning for fluid mechanics," Annu. Rev. Fluid Mech. **52**, 477 (2020).
[24] G. Y. C. Maceda, Y. Li, F. Lusseyran, M. Morzyński, and B. R. Noack, "Stabilization of the fluidic pinball with gradient-enriched machine learning control," J. Fluid Mech. **917**, A42 (2021).
[25] Y. Li, W. Cui, Q. Jia, Q. Li, Z. Yang, M. Morzyński, and B. R. Noack, "Explorative gradient method for active drag reduction of the fluidic pinball and slanted Ahmed body," J. Fluid Mech. **932**, A7 (2022).
[26] M. Wahde, *Biologically Inspired Optimization Methods: An Introduction* (WIT Press, 2008).

[27]Z. X. Qiao, G. Minelli, B. R. Noack, S. Krajnović, and V. Chernoray, "Multi-frequency aerodynamic control of a yawed bluff body optimized with a genetic algorithm," J. Wind Eng. Ind. Aerodyn. **212**, 104600 (2021).
[28]K. R. Cooper, "The effect of front-edge rounding and rear-edge shaping on the aerodynamic drag of bluff vehicles in ground proximity," SAE Paper No. 850288 (SAE International, Warrendale, PA, 1985).
[29]N. Kasagi, Y. Suzuki, and K. Fukagata, "Microelectromechanical systems–based feedback control of turbulence for skin friction reduction," Annu. Rev. Fluid Mech. **41**, 231 (2009).
[30]G. Pavia, M. Passmore, and M. Varney, "Low-frequency wake dynamics for a square-back vehicle with side trailing edge tapers," J. Wind Eng. Ind. Aerodyn. **184**, 417 (2019).
[31]J. H. Holland, *Adaptation in Natural and Artificial Systems* (MIT Press, 1992).
[32]T. Duriez, S. L. Brunton, and B. R. Noack, "Machine learning control—taming nonlinear dynamics and turbulence," in *Series Fluid Mechanics and Its Applications, No. 116* (Springer, Berlin, 2016).
[33]K. V. Mardia, T. J. Kent, and J. M. Bibby, *Multivariate Analysis, Probability and Mathematical Statistics* (Academic Press, 1979).
[34]Z. Wu, D. Fan, Y. Zhou, R. Li, and B. R. Noack, "Jet mixing optimization using machine learning control," Exp. Fluids **59**(8), 131 (2018).
[35]R. P. Littlewood and M. A. Passmore, "Aerodynamic drag reduction of a simplified squareback vehicle using steady blowing," Exp. Fluids **53**(2), 519 (2012).
[36]P. Gilliéron and A. Kourta, "Aerodynamic drag reduction by vertical splitter plates," Exp. Fluids **48**(1), 1 (2010).
[37]A. Okajima, "Strouhal numbers of rectangular cylinders," J. Fluid Mech. **123**, 379 (1982).
[38]H. L. Bai and M. M. Alam, "Dependence of square cylinder wake on Reynolds number," Phys. Fluids **30**(1), 015102 (2018).
[39]M. M. Zhang, L. Cheng, and Y. Zhou, "Closed-loop-controlled vortex shedding and vibration of a flexibly supported square cylinder under different schemes," Phys. Fluids **16**(5), 1439 (2004).